



Geothermal heat flux and basal melt rate in the Dome C region inferred from radar reflectivity and thermal modelling

Olivier Passalacqua^{1,2}, Catherine Ritz^{1,2}, Frédéric Parrenin^{1,2}, Stefano Urbini³, and Massimo Frezzotti⁴

¹Univ. Grenoble Alpes, LGGE, F-38401 Grenoble, France

²CNRS, LGGE, F-38401 Grenoble, France

³Istituto Nazionale di Geofisica e Vulcanologia, 00143 Roma, Italy

⁴ENEA, Centro Ricerche Casaccia, PO Box 2400, I-00100, Rome, Italy

Correspondence to: Olivier Passalacqua (olivier.passalacqua@univ-grenoble-alpes.fr)

Abstract. Basal melt rate is the most important physical quantity to be evaluated when looking for an old-ice drilling site, and it strongly depends on the geothermal heat flux, which is poorly known under the East Antarctic ice sheet. The wetness of the ice-bed interface can be assessed from radar echoes on the bedrock, considering that a wet bedrock has a stronger reflectivity than a dry one. But, as the basal conditions depends on the climatic forcing lagged by the thick ice, the basal ice may be cold today whereas it was in average temperate in the past. Accordingly, the risk of mismatch between present and past conditions must be evaluated, and more generally the geothermal heat flux and basal melt rate in the Dome C region, which is a promising old-ice target. Here, we run a 1D heat model over the last 800 ka in inverse mode to constrain the value of geothermal heat flux by assessing a critical ice thickness, i.e. the minimum ice thickness that would allow the local melting distribution at present. A regional map of the geothermal heat flux is then inferred on a 80 km × 130 km area, and shows a N-S-oriented gradient, with a value range of 48 – 60 mWm⁻². The forward model is then emulated by a polynomial function, to compute a time-averaged value of the basal melt rate, spatially variable over the region. Two main subregions appear to be free of basal melting because of the thin overlying ice, and a third one, north of Dome C, because of a low geothermal heat flux.

1 Introduction

The Dome C region (East Antarctica) has been a region of strong interest for the paleoclimatic science during the last decades, with two deep ice cores having been retrieved, including the oldest one ever dated (Lorius et al., 1979; Jouzel et al., 2007). Furthermore, the Dome C region has been identified as one possible candidate to host even older ice in its vicinity (Fischer et al., 2013; Van Liefferinge and Pattyn, 2013). To ensure a reliable age prediction of a future old-ice core site, the thermal conditions of the ice in the region must be well constrained, because the basal melting



strongly affects the possibility to get old ice by continuously removing the oldest layers (Rybak and Huybrechts, 2008).

25 Unfortunately, the geothermal heat flux (GHF), one of the key thermal parameter, remains poorly known in East Antarctica, because of the difficult access to the bedrock. The GHF is derived from borehole temperature gradients in the ground, for example in the dry valleys (Bücker et al., 2001), or by drilling through shallow ice-shelves (Morin et al., 2010) or sea ice (Schroeder et al., 2011), and then in the underlying sediments. The first direct measurement of GHF under an ice sheet was
30 obtained very recently below the Subglacial Lake Whillans (West Antarctic Ice Sheet), within sediment layers (Fisher et al., 2015). But in most cases the bedrock cannot be drilled, and GHF values are estimated from temperature profiles in ice core boreholes (Dahl-Jensen et al., 1998; Engelhardt, 2004). With this last method, more precise results are expected for cold basal conditions, since uncertainties affect the value of the basal melt rate in the case of temperate basal ice (Grinsted and
35 Dahl-Jensen, 2002), and then only a minimum value of GHF can be estimated.

Without any available temperature measurements, the value of the GHF has been estimated from geological considerations (Pollard et al., 2005; Llubes et al., 2006). Uniform values were assigned to large geologically homogeneous areas in Antarctica, but spatial variability of GHF occur at a much smaller scale. Two approaches based on geophysical information were proposed to provide maps
40 at a continent scale: from a seismic model of the crust and upper mantle (Shapiro and Ritzwoller, 2004), and from a crustal thickness model derived from magnetic field observation (Fox Maule et al., 2005; Purucker, 2013). These studies show that the GHF on the East Antarctic plateau is about $60 \pm 25 \text{ mW m}^{-2}$, which unfortunately is much too coarse an estimation to give any precise value at a specific location. Moreover, Terre Adélie and George V Land could form part of the Mawson
45 craton, which forms the southeast central part of Australia as well, and shows a high spatial variability in GHF (Carson et al., 2014). Even if the exact extent of this craton in Antarctica is not well known, the GHF in East Antarctica could contain hot spots, that could have a typical lengthscale of 10 km.

In radio echo sounding (RES) method, the presence of water at the ice-bed interface provides a remarkable increasing in amplitude of the reflected echoes that can be used to induce the basal conditions at a regional scale. As such, this methodology allowed to detect melting at the base of ice
50 sheets (Fujita et al., 2012; Oswald and Gogineni, 2012; Zirizzotti et al., 2012), and the mapping of subglacial lakes as well (Siegert et al., 2005). Schroeder et al. (2014) even inferred the value of the GHF needed to explain the observed pattern of radar echoes, using a collection of water routing models. They derived an average value of $114 \pm 10 \text{ mW m}^{-2}$ for the Thwaites Glacier catchment.
55 North of Dome C, basal melt rates have been estimated by fitting the vertical strains with dated internal layers, to constrain the energy budget of the ice (Carter et al., 2009). The uncertainty on the GHF was estimated $\pm 12 \text{ mW m}^{-2}$, which is a significative improvement compared to the previously available estimations, but is still quite large a value in the old-ice perspective. Moreover, their study area does not completely cover the main old-ice candidates (east and south-west of Dome C).



60 Without using internal layers, which are not available everywhere, we will follow a similar approach
to these two last studies, but adapted to the specific pattern of radar echoes under Dome C, where the
melting point is not reached everywhere.

Both ice thickness and GHF influence the thermal regime of the basal ice (temperate or cold). Ice
acts as an insulator, so that the thicker the ice is, the more heat is available for melting at the base
65 (Pattyn, 2010). Furthermore, the pressure melting point of the ice decreases linearly with the local
pressure, reducing the minimum ice thickness at which basal melting occur. To put it another way,
basal melting can be triggered by a higher ice thickness for a given GHF. In the Dome C region,
significant subglacial bedrock features make the ice thin enough to be interesting cold and dry, spots
commonly considered as interesting old-ice candidates in the glaciologist community (Fig. 1 - A, B, C
70 and D).

Based on radar equation, Zirizzotti et al. (2012) proposed a method to recognize the wet areas
using the Italian RES dataset collected around Dome C (<http://labet12.rm.ingv.it/antarctica/>). The
authors adopted a linear model of electromagnetic wave adsorption in the ice column, based on the
EDC ice core analysis, to account for the amplitude differences (in dB) between the ice surface
75 and the bottom echoes. In this paper, the thresholds considered to ascribe an echo to a wet or dry
basal contact were ≥ 7.7 dB and < 1 dB respectively. Figure 1 shows the distribution of dry and wet
areas under Dome C, revealing interesting patterns: (i) the Concordia trench is characterized by the
presence of wet points only, which is a consequence of the very thick ice; (ii) the tops of the two
main bedrock reliefs (candidate A and candidates B – C – D) appear to be dry; (iii) almost all the
80 northern points are dry, despite the very thick ice at this place; (iv) in between, and in particular
under the drilling site of EPICA, dry and wet points are scattered, showing no clear trend.

We emphasize that these observations show the bed conditions at present, whereas the historical
conditions all along the glacial/interglacial periods should be investigated to evaluate the quality
of a future old-ice drilling site. The absence of basal water today means a cold basal ice, but this
85 may simply be a consequence of the very strong temperature signal of the Last Glacial Maximum
(LGM) lagged by the thick ice. The present cold state may not be representative of the whole glacial-
interglacial periods, and thawing could have occurred in the past under different climatic conditions.
Hence, this paper primarily aims to assess the risk of past temperate conditions at places known to
be cold today. To this end, we present a 1D heat model forced by reconstructed climatic conditions,
90 and run it in two ways. First, in inverse mode to infer the value of the GHF in the Dome C region,
using radar echoes as observational constraints. Second, in forward mode to compute the average
past basal melt rate under the GHF inferred at the first step. We present an easy-to-use emulator
of the past basal melt rate, which is a convenient thermal boundary condition for future modelling
works, and key-criterion in the location of old-ice drilling sites.



95 2 Heat model

This section presents the heat model accounting for the relations between GHF, ice thickness and vertical advection of the ice. We first explain the main assumptions upon which the model is based. The areas on which these assumptions are valid are presented in section 3.

2.1 Model assumptions

100 2.1.1 1D-assumption

In a dome region, the horizontal velocities are very small (a few centimeters per year, (Vittuari et al., 2004)), so the horizontal advection terms can be neglected. Similarly, the deformational heat is several orders of magnitude smaller than the vertical advection term. Finally, due to the small aspect ratio (thickness/typical horizontal length), the temperature field is mainly vertically stratified, so that
105 the horizontal diffusion can be neglected as well. Thus, the heat balance of ice has dependences on the vertical direction only.

2.1.2 Water circulation at the base of the ice sheet

Since the wetness indicated by the basal echoes will be used as constraints on the inverse model, we first have to pinpoint the origin of the observed basal water. Whether the local ice is temperate and
110 the water comes directly from the thawed ice, or the local (cold) ice energy budget was imbalanced by the latent heat of a water flow coming from a temperate place, following the gradient of hydraulic potential. In the Dome C area, the ice surface is very flat and the hydraulic potential almost follows the bedrock heights, thus corresponding to the local maxima of hydraulic potential. Water cannot go upwards on these topographic features (Fig. 2). Hence, the water observed on the lee of a relief has
115 a local origin.

Could the dry areas observed on Fig. 1 correspond to a thawing ice whose meltwater would have flown away? Meltwater can be driven out by different types of hydrological networks: connected cavities (Lliboutry, 1968; Kamb, 1987) or efficient structured channels network (Röthlisberger, 1972). Weertman (1972) showed that these channels cannot form upstream of the hydrological network,
120 which is the case here, and would rather take the form of a film of water. Whatever the exact type of structure (film or cavities), basal melting is a continuous process that permanently feeds the hydrological network. Upstream of this network, the thawed water cannot be driven out faster than the melt rate, so that some water would always remain at the base of the ice. As a consequence, we suggest that the areas seen as dry in Fig. 2 effectively correspond to cold ice.

125 2.1.3 GHF spatial variability

According to the little that we know about the geology, we may assume that the GHF is uniform on a ~ 10 km-lengthscale. Under such an assumption, the presence of basal water is only the consequence



of a thicker ice, and not of GHF spatial variations. As such, thickness and reflectivity have to be locally correlated, and the model will be run for small areas where this correlation is reasonably
 130 ascertained.

2.2 Geometry and coordinate system

We consider here a one-dimensional vertical domain, oriented upwards along the z -axis. Instead of being set in the z -coordinates, the equations are expressed in reduced depth $\zeta = (s - z)/(s - b)$, s being the surface height, and b the bed height. In the ζ -coordinate system, the domain size
 135 remains the same whatever the ice thickness H , and no remeshing is needed in the resolution of the finite difference scheme. Therefore the ice thickness is a simple parameter evolving with time depending on the accumulation forcing at the surface. The thickness evolution is accounted for by the conceptual model of Parrenin et al. (2007), which emulates for the Dome C the 3D large scale simulations of Ritz et al. (2001). At each timestep, explicit expressions for the thickness and the
 140 bedrock elevation are solved, that depend on the accumulation rate and six tabulated parameters. The typical difference between ice thicknesses of glacial and interglacial periods is 150 m.

2.3 Heat equation

The heat balance of ice only depends on the vertical, and is written as follows in the ζ -coordinate system (Ritz et al., 1997):

$$145 \quad \frac{\partial T}{\partial t} = \frac{1}{\rho c D H^2} \frac{\partial}{\partial \zeta} \left(K \frac{\partial T}{\partial \zeta} \right) - u_{\zeta} \frac{\partial T}{\partial \zeta} \quad (1)$$

where K is the thermal conductivity of the ice, c its heat capacity, and D the relative density w.r.t. ice. The vertical velocity u_{ζ} accounts for the true ice velocity, but also for the evolution of the ice thickness, which changes the relationship between z and ζ .

2.4 Velocity model

150 The vertical advection of ice acts in the heat balance by transporting cold towards the bed. Instead of solving the equations of motion, it will be basically accounted for by a 1D shape function (Parrenin et al., 2007; Ritz, 1987):

$$\omega(\zeta) = 1 - \frac{p+2}{p+1} \cdot \zeta + \frac{1}{p+1} \cdot \zeta^{p+2} \quad (2)$$

$$155 \quad u_z = -\left(a - \frac{\partial H}{\partial t} - m\right) \cdot \omega(\zeta) - m \quad (3)$$

where the vertical velocity of ice in the z -coordinate system is called u_z , a is the surface accumulation rate and m the basal melt rate, taken positive when melting. The shape parameter p influences



the temperature profile, since it controls the vertical advection of ice from the surface to the base. The lower p , the more non linear vertical velocity profile. In practice, above a typical value of $p = 10$,
 160 the profile is very close to being linear (Fig. 3), and higher values of p do not change the profile significantly. The vertical velocity u_ζ in the ζ -coordinate system is then expressed as follows in the case of a shape function in a dome region (Parrenin et al., 2007):

$$u_\zeta = \frac{1}{H} \left(\frac{\partial H}{\partial t} (1 - \zeta - \omega(\zeta)) + m(1 - \omega(\zeta)) + a\omega(\zeta) \right) \quad (4)$$

which is equivalent to

$$165 \quad u_\zeta = \frac{1}{H} \left(-u_z + (1 - \zeta) \frac{\partial H}{\partial t} \right). \quad (5)$$

2.5 Ice thermal properties

The specific heat capacity and heat conductivity depend on the absolute temperature as follows (Cuffey and Paterson, 2010, p. 400):

$$c = 152.5 + 7.122 \cdot T \text{ [J K}^{-1} \text{ kg}^{-1}] \quad (6)$$

$$170 \quad K = 9.828 \cdot e^{-0.0057 \cdot T} \text{ [W m}^{-1} \text{ K}^{-1}] \quad (7)$$

The presence of firn at the surface of the ice lowers the conductivity at the ice sheet surface, and this must be accounted for (Cuffey and Paterson, 2010, p. 401):

$$K = \frac{2K_i \times D}{3 - D} \quad (8)$$

where K_i is the conductivity of the ice. The density profile of the firn layer is taken from Parrenin
 175 et al. (2007).

2.6 Boundary conditions at the bottom

At the ice/bed interface, the thermal conditions depend on whether the pressure melting point is reached or not. For thawing ice, the temperature simply equals the melting temperature. The melting temperature of pure ice linearly depends on the pressure following a Clapeyron law, for which
 180 the corresponding coefficient is $\mathcal{B} = 0.074 \text{ K Pa}^{-1}$. For glacier ice, a coefficient of 0.098 K Pa^{-1} was derived from measurements in Blue Glacier, Washington (Cuffey and Paterson, 2010; Harrison, 1972), accounting for the presence of saturated air dissolved in the ice. However, in ice sheets,



the air content is about $0.1 \text{ cm}^3/\text{g}$ (Martinerie et al., 1992), whereas the nitrogen saturates in ice at
 $\sim 2.6 \text{ cm}^3 \text{ g}^{-1}$ under a pressure of 27 MPa (Wiebe et al., 1932). The air is far from saturation for ice
 185 sheets. Only the partial pressure of air in the ice P' should be accounted for, so that the dependence
 of the melting temperature T_m on the pressure P (in MPa) and P' is expressed as (Ritz, 1992):

$$T_m = 273.16 - 0.074 \cdot P - 0.024 \cdot P' \quad (9)$$

In ice sheets, P' is of the order of 1 MPa. This is an unusual choice for such an important param-
 eter, but we argue that Eq.(9) is consistent with the temperature profile of the EPICA Dome C ice
 190 core, where the deepest measured temperature was 270.05 K at 3223 m, 50 m above the bedrock.
 The temperature profile can be extrapolated to the bedrock (similar to Dahl-Jensen et al. (2003) at
 North GRIP) to 271.04 K. The melting temperature computed with $\mathcal{B} = 0.098 \text{ K} \cdot \text{Pa}^{-1}$ would be
 0.8 K too low, whereas, it is found to be 270.96 K with Eq.(9). As the ice moves very slowly in the
 dome region, we assume that the pressure is only isostatic. Once the temperature field is computed,
 195 the melt rate at the bottom can be explicitly known by

$$m = \frac{1}{\rho L} \left(\Phi_g - \frac{K}{H} \frac{\partial T}{\partial \zeta} \Big|_{\zeta=1} \right) \quad (10)$$

where Φ_g is the GHF and L the latent heat of ice (J kg^{-1}). For cold basal ice, Eq. (10) is used as a
 Neumann boundary condition, equating m to zero.

2.7 Boundary condition at the ice surface

200 The atmospheric temperature forcing is continuously transferred through the whole column of ice,
 so that the present thermal conditions at the bed is the result of the whole climatic history. The
 atmospheric paleotemperatures are known over the last 800 ka from the δD measurements on the
 EPICA Dome C ice core (Jouzel et al., 2007). Here we use the model and notations of Parrenin
 et al. (2007), linking the isotope content of the ice to the temperature difference w.r.t. a reference
 205 temperature T^0 :

$$T = T^0 + \alpha \Delta \delta D_{\text{cor}} \quad (11)$$

The influence of the chosen value for α must be examined, since uncertainties affect our knowl-
 edge of the isotopic thermometer on long timescales in Antarctica, and α may vary by -10% to +20%
 (Jouzel et al., 2003). On top of the nominal value of $1/6.04 \text{ K}$, α will be given two additional values
 210 of 0.13 and 0.20, chosen so that the maximum temperature difference over climatic periods with the



nominal run is ± 2 K. Similarly, the corresponding accumulation rates are also taken from Parrenin et al. (2007), who considered an exponential accumulation model:

$$A = A^0 \exp(\beta \Delta \delta D_{\text{smo}}) \quad (12)$$

For Dome C, the value of the β coefficient was evaluated at 0.0156 ± 0.0012 by an inverse method
215 constrained by known age markers. Hence, we will check the sensitivity of our model for three
values of β (0.0138, 0.0156 and 0.0175). The two extreme values being chosen so that the maximum
accumulation difference over climatic periods with the nominal run is $\pm 0.25 \text{ cm a}^{-1}$, which is a
more intuitive way to express the sensitivity.

Regarding the choice of initial state, we considered that the duration needed for a step climatic
220 signal to reach the bedrock is ~ 10 ka, and ~ 100 ka to stabilize. As we do not know any true initial
state for the temperature profile in the past, we decided to run the model over the whole reconstructed
period (800 ka), so that the computation is independent of the initial state and the final vertical
temperature profile is as realistic as possible.

2.8 Numerical method

225 Equations are solved with a finite difference implicit scheme on a 50-element mesh, and the temporal
dependence of the model is solved on a 1000-year timestep. These values were selected as trade-offs
between result accuracy and computation speed.

The physical coupling between flow and heat content of the ice is accounted for by non linear
iterations, in which updated values of m , K and c are computed, till the temperatures do not show a
230 discrepancy larger than 10^{-5} K between two iterations. At each timestep, the heat equation is solved
for a boundary condition corresponding to the thermal state of the basal ice (temperate or cold). The
computed solution may be inconsistent with the imposed boundary condition, i.e. that the pressure
melting point may be exceeded (cold \rightarrow temperate), or the melt rate may become negative (temperate
 \rightarrow cold). In these cases, the equation is solved again with the new consistent boundary condition.

235 3 Measurement spots

We define the critical ice thickness H_c as the minimum ice thickness for which present basal melting
becomes possible for a given GHF and a given p . The model is run for increasing values of the GHF,
till the melting point is reached at present, so that we determine a unique tuple (H_c, p, Φ_g) . As the
unknown is the GHF, an estimation of this critical ice thickness is needed, and this is done in two
240 steps from the wet/dry map displayed on Fig. 1.

First, we determine spots for which ice thickness and reflectivity are correlated, i.e. for which the
top of bed reliefs are dry and their lees are wet (see Fig. 2). The melting starts to be physically possible
in between. Ten corresponding spots are selected (black rectangles in Fig. 1), that are hereafter



denoted by the indexes of their central point. The correlation between ice thickness and reflectivity
245 is shown on Fig. 4. For two spots (E4 and E6), the correlation is weak, but we retain them as they
are the only ones available in the central part of our study area.

Second, we evaluate the critical ice thickness for each spot. Along the radar line, going upwards
along a bed relief, we select the wet point for which the ice is the thinnest, and the dry point for which
the ice is the thickest. The same is done going downwards, so that four points are selected along the
250 radar line (black arrows on Fig. 2). The critical ice thickness H_c is estimated by the average of the
ice thickness measured at these points. The uncertainty on H_c is taken as the half of the standard
deviation of the four thicknesses, so that almost all the possible values ($H_c \pm 2\sigma$) range within the
extreme thicknesses measured at the considered spot. For the large spots C3 and C6, this operation
is done twice, on the two perpendicular radar lines going through them (radar lines C and 3, and C
255 and 6 respectively), so that eight dry/wet points are selected.

4 GHF inversion

The two main input parameters that influence the presence or absence of water on the bed are the
ice thickness H and the shape parameter p . Both of them are affected by uncertainties, and the
corresponding 2D-parameter space is explored with the heat model using a Monte-Carlo method
260 based on 200 (H, p) values spread along a Gaussian distribution. The critical thickness H_c measured
on the map is used as a prior for H . The shape parameter p cannot be less than -1 , and the inversion
is therefore done on the derived parameter p' :

$$p' = \ln(p + 1) \quad (13)$$

The prior value for p' is taken as a gaussian distribution of mean $\bar{p}' = 1.5$ and standard deviation
265 $\sigma_p = 0.3$ so that the corresponding values for p are mainly distributed between common values of 1
and 10. For a given present-day critical ice thickness H_c and a given p , the 1D heat model is run for
increasing values of Φ_g (by steps of 0.25 mW m^{-2}), and the first Φ_g value that allows melting for
the present time is selected as the local GHF. The thicker the ice, the lower the GHF needed to allow
for melting. The explored value range for Φ_g is $40\text{-}70 \text{ mW m}^{-2}$.

270 5 Results

5.1 Inverse mode: geothermal heat flux

The derived values of the mean GHF for the ten measurement spots are within a range of $48\text{-}60$
 mW m^{-2} (Table 1), and the highest values of the GHF are found south of Dome C. Given the
model assumptions, the inferred value for the GHF at two potential drilling sites (C6 and H1) are
275 respectively 59.3 ± 2.2 and $53.9 \pm 3.3 \text{ mW m}^{-2}$.



A kriging interpolation was carried out to evaluate the GHF between the evaluated spots. Unfortunately, they are scarce (ten points only), and unevenly distributed within the study area. As such, the computed experimental variogram was poorly described, and our confidence in the computed kriging standard deviation is low. Moreover, the presence of local variability at a scale of a few tens
280 of kilometers cannot be excluded, so that the validity of such an interpolation is limited. However, we highlight the importance of such a map to show the regional trend that can be expected around Dome C.

Figure 5 shows the interpolation between the ten spots, in which the GHF field smoothly evolves along a N-S gradient, with a typical norm of $0.1 \text{ mW m}^{-2} \text{ km}^{-1}$. At the two sites where the correlation between reflectivity and ice thickness is weak (E4 and E6), the inferred values of the GHF
285 do not mismatch with the N-S gradient, even if the value at E4 seems significantly lower than its neighbours. Given that the kriging standard deviation does not account for the uncertainty on the GHF estimation at the spots, the GHF at the EPICA drilling site is estimated at $54.5 \pm 3.5 \text{ mW m}^{-2}$.

5.2 Forward mode: emulator of the basal melt rate averaged over the last 400 000 years

290 Computing an average value of the basal melt rate is needed to assess the risk of losing the oldest ice layers during the glacial/interglacial periods. To do so, the GHF field inferred at the previous step is now used as an input for the heat model. Running it transient allows the computation of the basal melt rate at each time step, which is done for a large range of H and p values, while α and β are kept at $1/6.04$ and 0.0156 respectively. Because of the uncertainty on the initial state, the accuracy of our
295 temperature profile is unclear during the first glacial cycles, and we average the computed melt rate over the last 400 ka only.

The empirical relationship that links the average melt rate to the model parameters appears to be very regular (Fig.6). The slope of the isomelt contour lines shows a close equivalence between GHF and ice thickness ($1 \text{ mW m}^{-2} \Leftrightarrow 60 \text{ m}$). The sensitivity of the melt rate on p seems to be equivalent
300 to a range of 2 mW m^{-2} of GHF. An additional flux of 1 mW m^{-2} correspond to an increased melt rate of 0.09 mm a^{-1} . To account for this relationship by a multivariable polynomial, it seems natural to make m depend linearly on Φ_g , and quadratically on H and p . Over the positive-melt-value domain, we computed by a least-square minimization method the following relation:

$$305 \quad m = -5.148 \times 10^{-7} H^2 + 4.688 \times 10^{-3} H + 89.519 \Phi_g + 3.08 \times 10^{-3} p^2 - 5.887 \times 10^{-2} p - 14.335. \quad (14)$$

The performance of the emulator is assessed by comparing the melt rate output from the thermal model with the one computed with the emulator. The average absolute error is 0.014 mm a^{-1} , and the corresponding standard deviation is 0.016 mm a^{-1} , so that the errors due to the emulator are



significantly lower than the corresponding uncertainties due to the GHF and p . This polynomial
 310 function is thus considered precise enough for our purpose.

We now call $\hat{\Phi}_g$ the GHF field and $\hat{\Phi}_g^m$ the one based on the average values derived at the spots.
 The averaged basal melt rate in the past was inferred for two pessimistic cases: *a*) a high value of
 the GHF ($\hat{\Phi}_g^m + 2\sigma_\Phi$), and *b*) a low value of p' ($\bar{p}' - 2\sigma_p$), leading to little advection of cold ice. As
 Φ_g and p are not independent within the inversion process, the values of p and $\hat{\Phi}_g$, for *a*) and *b*)
 315 respectively, are basically chosen as their expected values under the condition chosen for the other
 variable. They are computed on the joint distribution given by inversion step as follows, where Φ_g^i is
 the GHF at the spot i , and $\bar{\Phi}_g^i$ its central value inferred by the inversion.

$$a) E[p | \Phi_g^i \geq \bar{\Phi}_g^i + 2\sigma_\Phi, \forall i] = 4.4 \quad (15)$$

$$b) E[\Phi_g^i | p' \leq \bar{p}' - 2\sigma_p] \simeq \bar{\Phi}_g^i - 1.1 \quad (16)$$

The figure 8 shows that the basal melt rate goes up to 1.0 mm a^{-1} where ice is very thick, and
 vanishes over several spots. The candidates A, B, C and D appear to be melt-free, which was expected,
 since they benefit from a relatively lower ice thickness. Less expected is the presence of a poten-
 tially melt-free area sixty kilometers north from Dome C (point N8). The ice is quite thick there
 ($\sim 3300 \text{ m}$), but the computed GHF is low enough to prevent ice from melting. For high GHF values
 325 (case *a*)), the basal melt rate is generally increased by a typical amount of $\sim 0.2 \text{ mm a}^{-1}$, in compar-
 ison with case *b*). Hence, the extend of the melt-free spots is drastically decreased, however they still
 remain under this high GHF pessimistic assumption. The temporal evolution of the basal melt rate
 is also shown for two (H_c, Φ_g) temperate configurations, leading to the same average value (Fig. 7).
 The difference between minimum and maximum value of the basal melt rate is 0.6 mm a^{-1} for a
 330 2770 m-thick ice, but additionnal 500 m of ice dampens this amplitude by a half, and smoothes out
 high frequencies. The difference between present melt rates and maximum past values suggest that,
 more generally, it is possible that present cold basal ice was melting during the warmest periods.

5.3 Sensitivity tests

The influence of the climatic forcing is now investigated, by running the model for different slopes
 335 of the isotopic thermometer. The results for the GHF obtained by the inverse method are shifted
 positively by 1.4 mW m^{-2} for $\alpha = 0.20$ and negatively for $\alpha = 0.13$. However, the average basal
 melt rate is changed at the opposite by 0.1 mm a^{-1} , so that the final difference in the inferred melt
 rate is only 0.04 mm a^{-1} (Table 2). Because the parameter α affects both the derivation of the GHF
 on the spots and the model melt rate, the two steps partly compensate each other when producing
 340 the melt rate map.



For extreme values of the β coefficient (accumulation model), the results are shifted positively by 0.3 mW m^{-2} for $\beta = 0.0138$ and negatively for $\beta = 0.175$. Similarly to α , the average basal melt rate is changed at the opposite by 0.01 mm a^{-1} , so that the final difference in the inferred melt rate is only 0.02 mm a^{-1} .

345 The accumulations reconstructed at the Dome itself were equally used for the whole region, whereas spatial variations surely affect the surface accumulation rate around Dome C (Frezzotti et al., 2005). The sensitivity of our model to a $\pm 10\%$ variation of the surface accumulation results in a $\pm 0.3 \text{ mW m}^{-2}$ difference for the GHF, and to an opposite $\pm 0.08 \text{ mm a}^{-1}$ for basal melt rate. The final sensitivity of the basal melt rate is thus $\pm 0.05 \text{ mm a}^{-1}$. A higher accumulation rate results
350 in a lower basal melt rate, which is expected.

Given that the expression of the pressure melting point is an unusual choice in glaciology (Eq. 9), the inverse method was reiterated with a more common value ($\mathcal{B} = 0.098 \text{ K.Pa}^{-1}$) as a test. The inferred GHF values were found to be shifted by -0.6 mW m^{-2} compared to our expression. The order of magnitude of the results remains the same whatever the expression for the pressure melting
355 point, as well as the regional pattern of GHF.

5.4 Forward mode: emulator of the critical ice thickness

The method performance is finally assessed by comparing modelled present melting areas to the ones observed by Zirizzotti et al. (2012). The relation between critical ice thickness and GHF is emulated by a one-variable polynom for $p = 2$:

$$360 \quad H_c = 101327.4\Phi_g^2 - 170906\Phi_g + 9486.0 \quad (17)$$

This allows to compute the difference between critical ice thickness and the present ice thickness (Bedmap2), so that negative values correspond to melting areas, and positive values to melt-free areas. We intend to broadly mimick the wet/dry pattern in areas where no critical thickness was measured (north of Dome C), so we tune on purpose the imposed GHF field, within the uncertainty
365 range. The map presented on Fig. 9 was build for $\hat{\Phi}_g^m - 1 \text{ mW m}^{-2}$. Superimposed with the observation data, much of the map is quite well assigned, even far from the ten measurement spots. Despite the lack of accuracy of the thickness description, many small-scale structures are well described (e.g. E6-7, G4, G-H8, H6, I9, L7-8). The steeper the bed, the sharper the limit between melting and no-melting areas; this limit appears very smooth in the central part. If this threshold between
370 temperate and cold ice is somewhat offset locally, the spatial pattern of dry/wet areas is however often respected in Fig. 9 (e.g. G-H8, G9, J6). Given the uncertainties, only one spot appears to be undoubtedly inconsistent (F8), but this is explained by a difference of vertical accuracy of the data (local gap of $\sim 100 \text{ m}$ between Bedmap2 and the radar data).



The heat model allow an easy detection at the base of the ice of the very strong climatic signal of
375 the LGM, and the corresponding time lag for basal temperature appears to linearly depend on the ice
thickness for the range 2700-3500 m (Fig. 9) by the following relation

$$\Delta t = 10H - 16610. \quad (18)$$

The isocontours of the time lag Δt are simply parallel to the thickness contours, but allow a
temporal interpretation of the wet/dry patterns. Around 10 ka are required for the signal to reach
380 the tops of bed reliefs, but almost twice this value for a 3400 m-thick ice. Hence, considering the
duration of a deglaciation, the thermal state of the basal ice corresponds to very different climatic
periods depending on the overburden ice thickness.

6 Discussion

6.1 Method validity

385 6.1.1 Model assumptions

Around Dome C, ice may flow over a hilly bedrock, and the velocity profile is not necessarily as
smooth as a 1D synthetical shape function. However, the energy budget at the base of the ice actually
depends on the total advection of cold from the top, not on the particular shape of the vertical velocity
profile. Using a synthetic profile is just a convenient way to account for a realistic transport of cold
390 towards the bed.

Some of the given confidence intervals are quite low (E4, E6, L7 and N8), and this is a conse-
quence of the tiny altitude difference measured on Fig. 1 between the highest wet points and the
lowest dry ones for a given spot. Since the correlation between ice thickness and reflectivity was
weak, the confidence intervals at E4 and E6 are probably underestimated, and some local effects
395 may not have been accounted for in this study (e.g. small relief and GHF variabilities).

We cannot exclude any assignment error of the dry points, if ever a small water film is present but
not detected. If so, we would only be able to assess a lower boundary for the GHF. Water remaining
at the base enables basal sliding, which can be suspected by observing the slope of the ice surface.
The surface slope is the source of motion, so that no sliding enhances a steeper slope, and sliding,
400 a smaller slope. Most of our measurement spots are standing on slopes locally steeper than the
regional slope, so that it is likely that sliding does not occur there, giving an additional hint that the
base is cold (Table 1). If the basal ice is anyway temperate despite this favourable clue, the absence
of detection of the meltwater likely means that the water film is very thin and the melt rate is very
small. The average inferred GHF would be only offset by a small amount, and the regional GHF
405 gradient would be unchanged.



6.1.2 Sensitivity to parameters

The sensitivity of our results to the climatic forcing shows that the confidence interval on the GHF at the 10 spots could be larger than presented so far, possibly by $\sim 2 \text{ mW m}^{-2}$. However, for the archiving process, the truly important parameter is the basal melt rate, which is much less sensitive.

410 For example, a lower α correspond to a lower inferred GHF (inverse run), but the average melt rate is higher for the same GHF (direct run). The latter compensates two thirds of the effect of the former, so that the melt rates computed for the ten measurement spots are quite robust to our lack of knowledge on the climatic forcing.

As the present surface accumulation pattern shows a N-S gradient, we wonder if our GHF gradient
415 could come from an artefact of our method, which does not account for the spatial variations of accumulation. As the sensitivity of the GHF on the surface accumulation is rather limited, accounting for its variations would not radically change our results. Furthermore, we do not know how stable is the pattern of accumulation over the glacial/interglacial periods, so that assuming its stability would results in unnecessary additionnal uncertainties.

420 6.1.3 Consistency with published data and measurements

Our GHF values are comparable to the ones inferred by Fox Maule et al. (2005) and Purucker (2013), but, as their uncertainties are quite large, they cannot be considered as a litmus test. For the northern part of our domain, the relatively low values of GHF ($\sim 50 \text{ mW m}^{-2}$ or less) is closely consistent with the estimation of Carter et al. (2009) at the same place, except on a bed relief (candidate D),
425 where they find a positive heat flux anomaly and a high melt rate on its flanks ($\sim 2.5 \text{ mm a}^{-1}$). The heat anomaly cannot be induced with our method, since the GHF is interpolated at this place. This illustrates that our method is reasonably reliable where we do have an estimation of the critical thickness (corresponding to interesting dry, low-reflective cold spots), and at least describes a GHF regional background elsewhere.

430 At the EPICA drilling site, we compute an average melt rate of $0.32 \pm 0.25 \text{ mm a}^{-1}$, and this value seems to be slightly lower than, but however consistent with the value of $0.56 \pm 0.19 \text{ mm a}^{-1}$ already inferred by Parrenin et al. (2007), which was computed over longer timescales. The range of possible basal melt rates inferred from our method seems realistic enough to contain its effective local value, at a place where there is no observation of the critical thickness yet. The basal melt rate
435 inferred for the different old-ice candidates, where we have observations of H_c , is thus reliable. The ice temperature gradient measured in the borehole is $-0.022655 \text{ K m}^{-1}$ at the base, corresponding to a net heat flux of 48 mW m^{-2} going into the ice. The present corresponding amount of melting for our interpolated GHF is 0.7 mm a^{-1} , which seems consistent with the time-averaged value of Parrenin et al. (2007) regarding the fact that the deglaciation signal has already reached the bedrock
440 for 4 ka.



6.1.4 Structure of the GHF field

In our point-by-point method, there is no horizontal regularization constraints to make the GHF being realistic at a regional scale. Yet, the inferred heat flow at the ten spots shows a certain spatial correlation, which is a good omen of plausibility. More fundamentally, we can explain at first order a relatively complex pattern of wet/dry areas on a whole region with a single physical key (a smoothly-varying GHF field) without any 2D water routing model, or horizontal heat transport depending on both ice flow and bedrock topography. This application of the parcimony principle of Occam's razor supports the validity of our 1D approach, and means that the main physical mechanisms have been accounted for. Of course, a higher-dimension ice flow and hydrological model, over a refined bedrock, would be necessary to go one step beyond to describe the water variability more closely, but more assumptions regarding the model parameters would also lead to higher model uncertainties. The GHF confidence intervals given for the surroundings of Dome C are now about five to ten times lower than the ones previously available. In the frame of the oldest-ice project, we suggest that $\hat{\Phi}_g^m + 2\sigma_{\Phi}$ is a realistic higher boundary for the local GHF value.

6.2 Interpretation

The basal melt rate map (averaged over the last 400 000 years) shows that the old-ice candidates appear to be melt-free all along glacial/interglacial periods. On the contrary, the northern part of Dome C is broadly a thawing area, whereas Zirizzotti et al. (2012) observed no presence of water, in spite of the local thick ice. In this region, the climatic signal of the last deglaciation has reached the bedrock later than in regions of thinner ice (Fig 9, contour lines). If the basal ice was cold at the LGM, the pressure melting point has not been reached yet since the deglaciation signal has just reached the bed for the last ~ 2000 years. For thinner ice, the deglaciation signal is close to be already past; if the basal ice is still cold now, it should be the case over the whole glacial/interglacial periods as well. The time lag for the climatic signal to reach the bed then appears to be a self-sufficient parameter to detect cold-based areas on long time scales. However, this only criteria would not be sufficient to detect all of these areas, or to discuss their spatial extent.

6.3 Consequences for the old-ice targets

As expected, the regions where the basal ice is supposed to be cold over the glacial/interglacial periods are the candidate A and the candidates B, C and D. These three last places may undergo a lower GHF than candidate A and could be better places to exclude the possibility of basal melting. However, they are separated from the topographic dome by the Concordia trench. The deep ice that could be drilled at these places have likely crossed the trench, and the stratigraphy may have been affected by this topographically-disturbed region. Furthermore, the ice velocity is probably higher than over the candidate A because of the steeper slope starting from the dome, and this may



475 enhance basal disturbance. Given the confidence intervals, the GHF difference with candidate A
is not significant enough to make candidates B, C and D first choices, but they remain spots of great
interest. Three-dimensional modelling will be performed to study the regional ice flow towards these
sites in more details.

Our study also suggests that a certain spot in the northern part of Dome C may undergo a low
480 enough GHF to prohibit basal melt rate over long time scales. As the ice is significantly thicker
than at other previously considered candidates, a very old ice could be retrieved with a much better
resolution than elsewhere. Considering that the clue leading to this conclusion is not cross-checked
(one observation only), we emphasize the importance of carrying out additional survey to assess the
validity of this statement (e.g. ground/airborne radar).

485 Finally, the evolution of the benthic $\delta^{18}\text{O}$ past sea level proxy (Lisiecki and Raymo, 2005), and
its close similarity with the one of the EDC reconstructed temperatures, show that the mean air
temperature at Dome C was probably higher by $\sim 2\text{ K}$ before -800 ka than after. As a consequence,
the mean basal melt rate was probably higher by 0.1 mm a^{-1} as well. Even if we conclude this study
on favorable statements, we should bear in mind that basal ice has maybe undergone little melting
490 on tops and flanks of bed reliefs during the Mid-Pleistocene.

7 Conclusions

The geothermal heat flux is a poorly constrained geophysical parameter in Antarctica, despite its
crucial influence on the ice flow properties and old-ice archiving. Around Dome C, the available
continental estimations are currently of limited benefit, and we lack a more precise local estimation.
495 We have presented a simple inverse method based on a 1D heat model, constrained by amplitude
analysis of RES echoes recorded at ice/bedrock interface trying to discriminate wet and dry areas on
the bed. Assuming that the GHF is locally uniform, the presence of basal water is only a function
of ice thickness. The critical ice thickness, for which the pressure melting point is reached today,
is inferred from wet/dry thresholds used in the analysis of RES amplitude data (Zirizzotti et al.,
500 2012). The heat model, accounting for the whole history of the ice (temperature, accumulation and
thickness evolution), is inverted for this critical thickness, to retrieve the value of the GHF and of the
time-averaged basal melt rate for ten spots around Dome C.

Our method is valid in dome areas, where horizontal advection and diffusion can be neglected, but
its principle could be adapted for other regions with a more complex physical scheme. However, it
505 assumes that the origin of the observed basal water is local, so that it is better suited for flat regions,
where there is no upwards water transport on the bed reliefs. Moreover, in places where horizontal
ice flow is significant, deformational heat should be accounted for in the energy balance of ice.

Furthermore, we show that the role of the ice thickness appears to be dual. Of course, in average,
it limits the heat diffusion towards the surface and enhances basal melting. But under an evolving



510 climate, it lags the temperature forcing, so that the base of a thin ice is more sensitive to climate evolution, while the base of a thick ice has just begun to be under deglaciation and may still be cold today. Hence, as the LGM was one of the coldest climatic conditions ever recorded, the lag effect of the ice thickness must absolutely be accounted for to correctly interpret present basal conditions.

515 The interpolated map of the GHF shows a regional gradient, oriented North-South. Where no critical thicknesses have been measured, the GHF values are consistent with the pattern of dry and wet points, in particular in the northern region, which appears to be dry today, and hosts a site of old ice potential. All the previously considered old-ice candidates are very likely cold-based, or to have undergone very little basal melting. We hope this work will provide the community with helpful and realistic thermal boundary conditions for any ice flow modelling in the Dome C region.



520 References

- Bamber, J., Gomez-Dans, J., and Griggs, J.: Antarctic 1 km digital elevation model (DEM) from combined ERS-1 radar and ICESat laser satellite altimetry, National Snow and Ice Data Center, Boulder, Colorado, 2009.
- Bücker, C., Jarrard, R., and Wonik, T.: Downhole temperature, radiogenic heat production, and heat flow from the CRP-3 drillhole, Victoria Land Basin, Antarctica, *Terra Antarctica*, 8, 151–160, 2001.
- 525 Carson, C. J., McLaren, S., Roberts, J. L., Boger, S. D., and Blankenship, D. D.: Hot rocks in a cold place: high sub-glacial heat flow in East Antarctica, *Journal of the Geological Society*, 171, 9–12, doi:10.1144/jgs2013-030, 2014.
- Carter, S. P., Blankenship, D. D., Young, D. A., and Holt, J. W.: Using radar-sounding data to identify the distribution and sources of subglacial water: application to Dome C, East Antarctica, *Journal of Glaciology*, 55, 1025–1040, 2009.
- 530 Cuffey, K. M. and Paterson, W. S. B.: *The physics of glaciers*, Academic Press, 2010.
- Dahl-Jensen, D., Mosegaard, K., Gundestrup, N., Clow, G., Johnsen, S., Hansen, A., and Balling, N.: Past Temperatures Directly from the Greenland Ice Sheet, *Science*, 282, 268, doi:10.1126/science.282.5387.268, 1998.
- 535 Dahl-Jensen, D., Gundestrup, N., Prasad Gogineni, S., and Miller, H.: Basal melt at NorthGRIP modeled from borehole, ice-core and radio-echo sounder observations, *Annals of Glaciology*, 37, 207–212, 2003.
- Engelhardt, H.: Ice temperature and high geothermal flux at Siple Dome, West Antarctica, from borehole measurements, *Journal of Glaciology*, 50, 251–256, 2004.
- 540 Fischer, H., Severinghaus, J., Brook, E., Wolff, E., Albert, M., Alemany, O., Arthern, R., Bentley, C., Blankenship, D., Chappellaz, J., Creyts, T., Dahl-Jensen, D., Dinn, M., Frezzotti, M., Fujita, S., Gallee, H., Hindmarsh, R., Hudspeth, D., Jugie, G., Kawamura, K., Lipenkov, V., Miller, H., Mulvaney, R., Parrenin, F., Pattyn, F., Ritz, C., Schwander, J., Steinhage, D., van Ommen, T., and Wilhelms, F.: Where to find 1.5 million yr old ice for the IPICS "Oldest-Ice" ice core, *Climate of the Past*, 9, 2489–2505, doi:10.5194/cp-9-2489-2013, 2013.
- 545 Fisher, A. T., Mankoff, K. D., Tulaczyk, S. M., Tyler, S. W., Foley, N., et al.: High geothermal heat flux measured below the West Antarctic Ice Sheet, *Science advances*, 1, e1500093, doi:10.1126/sciadv.1500093, 2015.
- Fox Maule, C., Purucker, M. E., Olsen, N., and Mosegaard, K.: Heat flux anomalies in Antarctica revealed by satellite magnetic data, *Science*, 309, 464–467, doi:10.1126/science.1106888, 2005.
- 550 Fretwell, P. and coauthors: Bedmap2: improved ice bed, surface and thickness datasets for Antarctica, *The Cryosphere*, 7, 375–393, doi:10.5194/tc-7-375-2013, 2013.
- Frezzotti, M., Pourchet, M., Flora, O., Gandolfi, S., Gay, M., Urbini, S., Vincent, C., Becagli, S., Gragnani, R., Proposito, M., and others: Spatial and temporal variability of snow accumulation in East Antarctica from traverse data, *Journal of glaciology*, 51, 113–124, <http://www.ingentaconnect.com/content/igsoc/jog/2005/00000051/00000172/art00011>, 2005.
- 555 Fujita, S., Holmlund, P., Matsuoka, K., Enomoto, H., Fukui, K., Nakazawa, F., Sugiyama, S., and Surdyk, S.: Radar diagnosis of the subglacial conditions in Dronning Maud Land, East Antarctica, *The Cryosphere*, 6, 1203–1219, 2012.



- Grinsted, A. and Dahl-Jensen, D.: A Monte Carlo-tuned model of the flow in the NorthGRIP area, *Annals of Glaciology*, 35, 527–530, 2002.
- Harrison, W.: Temperature of a temperate glacier, *Journal of Glaciology*, 11, 15–29, 1972.
- Jouzel, J., Vimeux, F., Caillon, N., Delaygue, G., Hoffmann, G., Masson-Delmotte, V., and Parrenin, F.: Magnitude of isotope/temperature scaling for interpretation of central Antarctic ice cores, *Journal of Geophysical Research (Atmospheres)*, 108, 4361, 2003.
- 565 Jouzel, J., Masson-Delmotte, V., Cattani, O., Dreyfus, G., Falourd, S., Hoffmann, G., Minster, B., Nouet, J., Barnola, J. M., Chappellaz, J., Fischer, H., Gallet, J. C., Johnsen, S., Leuenberger, M., Loulergue, L., Luethi, D., Oerter, H., Parrenin, F., Raisbeck, G., Raynaud, D., Schilt, A., Schwander, J., Selmo, E., Souchez, R., Spahni, R., Stauffer, B., Steffensen, J. P., Stenni, B., Stocker, T. F., Tison, J. L., Werner, M., and Wolff, E. W.: Orbital and Millennial Antarctic Climate Variability over the Past 800,000 Years, *Science*, 317, 793–796, doi:10.1126/science.1141038, 2007.
- 570 Kamb, B.: Glacier surge mechanism based on linked cavity configuration of the basal water conduit system, *Journal of Geophysical Research*, 92, 9083, doi:10.1029/JB092iB09p09083, <http://doi.wiley.com/10.1029/JB092iB09p09083>, 1987.
- Lisiecki, L. E. and Raymo, M. E.: A Pliocene-Pleistocene stack of 57 globally distributed benthic $\delta^{18}\text{O}$ records, *Paleoceanography*, 20, 2005.
- 575 Lliboutry, L.: General theory of subglacial cavitation and sliding of temperate glaciers, *Journal of Glaciology*, 7, 21–58, 1968.
- Lubes, M., Lanseau, C., and Rémy, F.: Relations between basal condition, subglacial hydrological networks and geothermal flux in Antarctica, *Earth and Planetary Science Letters*, 241, 655–662, doi:10.1016/j.epsl.2005.10.040, 2006.
- 580 Lorius, C., Merlivat, L., Jouzel, J., and Pourchet, M.: A 30,000-yr isotope climatic record from Antarctic ice, *Nature*, 280, 644–648, 1979.
- Martinier, P., Raynaud, D., Etheridge, D. M., Barnola, J.-M., and Mazaudier, D.: Physical and climatic parameters which influence the air content in polar ice, *Earth and Planetary Science Letters*, 112, 1–13, 1992.
- 585 Morin, R., Williams, T., Henrys, S., Magens, D., Niessen, F., and Hansaraj, D.: Heat Flow and Hydrologic Characteristics at the AND-1B borehole, ANDRILL McMurdo Ice Shelf Project, Antarctica, *Geosphere*, 6, 370–378, doi:10.1130/GES00512.1, 2010.
- Oswald, G. K. and Gogineni, S.: Mapping Basal Melt Under the Northern Greenland Ice Sheet, *IEEE Transactions on Geoscience and Remote Sensing*, 50, 585–592, doi:10.1109/TGRS.2011.2162072, 2012.
- 590 Parrenin, F., Dreyfus, G., Durand, G., Fujita, S., Gagliardini, O., Gillet, F., Jouzel, J., Kawamura, K., Lhomme, N., Masson-Delmotte, V., et al.: 1-D-ice flow modelling at EPICA Dome C and Dome Fuji, East Antarctica, *Climate of the Past*, 3, 243–259, 2007.
- Pattyn, F.: Antarctic subglacial conditions inferred from a hybrid ice sheet/ice stream model, *Earth and Planetary Science Letters*, 295, 451–461, doi:10.1016/j.epsl.2010.04.025, 2010.
- 595 Pollard, D., DeConto, R. M., and Nyblade, A. A.: Sensitivity of Cenozoic Antarctic ice sheet variations to geothermal heat flux, *Global and Planetary Change*, 49, 63–74, doi:10.1016/j.gloplacha.2005.05.003, 2005.



- Purucker, M.: Geothermal heat flux data set based on low resolution observations collected by the CHAMP satellite between 2000 and 2010, and produced from the MF-6 model following the technique described in Fox Maule et al.(2005), See <http://websrv.cs.umt.edu/isis/index.php>, 2013.
- 600 Ritz, C.: Time dependent boundary conditions for calculation of temperature fields in ice sheets, *IAHS Publ.*, 170, 207–216, 1987.
- Ritz, C.: Un modèle thermo-mécanique d'évolution pour le bassin glaciaire Antarctique Vostok-Glacier Byrd: Sensibilité aux valeurs des paramètres mal connus., Ph.D. thesis, Université Joseph-Fourier-Grenoble I, 1992.
- Ritz, C., Fabre, A., and Letréguilly, A.: Sensitivity of a Greenland ice sheet model to ice flow and ablation parameters: consequences for the evolution through the last climatic cycle, *Climate Dynamics*, 1, 605 doi:10.1007/s003820050149, 1997.
- Ritz, C., Rommelaere, V., and Dumas, C.: Modeling the evolution of Antarctic ice sheet over the last 420,000 years: Implications for altitude changes in the Vostok region, *Journal of Geophysical Research*, 106, 31, 2001.
- 610 Rybak, O. and Huybrechts, P.: Sensitivity of the EDML ice core chronology to the geothermal heat flux, *Materialy Glatsiologicheskikh issledovaniy (Data of glaciological studies)*, 105, 35–40, 2008.
- Röthlisberger, H.: Water pressure in intra- and subglacial channels, *Journal of Glaciology*, 11, 177–203, 1972.
- Schroeder, D., Blankenship, D., Young, D., and Quartini, E.: Evidence for elevated and spatially variable geothermal flux beneath the West Antarctic Ice Sheet, in: *Proceedings of the National Academy of Science*, 615 vol. 111, pp. 9070–9072, 2014.
- Schroeder, H., Paulsen, T., and Wonik, T.: Thermal properties of the AND-2A borehole in the southern Victoria Land Basin, McMurdo Sound, Antarctica, *Geosphere*, 7, 1324–1330, doi:10.1130/GES00690.1, 2011.
- Shapiro, N. M. and Ritzwoller, M. H.: Inferring surface heat flux distributions guided by a global seismic model: particular application to Antarctica, *Earth and Planetary Science Letters*, 223, 213–224, 620 doi:10.1016/j.epsl.2004.04.011, 2004.
- Siebert, M. J., Carter, S., Tabacco, I., Popov, S., and Blankenship, D. D.: A revised inventory of Antarctic subglacial lakes, *Antarctic Science*, 17, 453–460, doi:10.1017/S0954102005002889, 2005.
- Van Liefferinge, B. and Pattyn, F.: Using ice-flow models to evaluate potential sites of million year-old ice in Antarctica, *Climate of the Past Discussions*, 9, 2859–2887, doi:10.5194/cpd-9-2859-2013, 2013.
- 625 Vittuari, L., Vincent, C., Frezzotti, M., Mancini, F., Gandolfi, S., Bitelli, G., and Capra, A.: Space geodesy as a tool for measuring ice surface velocity in the Dome C region and along the ITASE traverse, *Annals of Glaciology*, 39, 402–408, 2004.
- Weertman, J.: General theory of water flow at the base of a glacier or ice sheet, *Reviews of Geophysics*, 10, 287–333, 1972.
- 630 Wiebe, R., Gaddy, V., and Heinss Jr, C.: Solubility of nitrogen in water in 250c from 25 to 1000 atmospheres, *Industrial & Engineering Chemistry*, 24, 927–927, 1932.
- Zirizzotti, A., Cafarella, L., and Urbini, S.: Ice and Bedrock Characteristics Underneath Dome C (Antarctica) From Radio Echo Sounding Data Analysis, *IEEE Transactions on Geoscience and Remote Sensing*, 50, 37–43, doi:10.1109/TGRS.2011.2160551, 2012.



Table 1. Physical parameters, observed (critical thickness $H_c \pm 1\sigma$ [m], ratio of local surface slope to regional surface slope (ICESat)) and inverted (GHF $\Phi_g \pm 1\sigma_\Phi$ [mW m^{-2}]). The surface slopes are computed on the 3km and 10km-radius circles centered on each spot, on which the surface DEM (Bamber et al., 2009) is fitted by a biquadratic function.

| Spot | H_c | $\Phi_g \pm \sigma_\Phi$ | Surf. slope ratio |
|------|----------------|--------------------------|-------------------|
| B9 | 3157 ± 46 | 55.5 ± 0.9 | 1.03 |
| C3 | 2926 ± 75 | 59.8 ± 1.5 | 1.20 |
| C6 | 2957 ± 111 | 59.3 ± 2.2 | 1.09 |
| E4 | 3181 ± 46 | 55.2 ± 0.9 | 0.97 |
| E6 | 3124 ± 17 | 56.1 ± 0.5 | 2.01 |
| H1 | 3249 ± 197 | 53.9 ± 3.3 | 1.80 |
| L4 | 3319 ± 209 | 53.2 ± 2.9 | 1.37 |
| L7 | 3408 ± 48 | 51.6 ± 0.8 | 1.46 |
| N4 | 3662 ± 92 | 48.1 ± 1.2 | 1.27 |
| N8 | 3698 ± 49 | 47.6 ± 0.7 | 1.42 |

Table 2. Sensitivity of the GHF (inverse runs, [mW m^{-2}]) and basal melt rate (forward runs, [mm a^{-1}]) to input parameters. The last column accounts for the sensitivity on the whole method (inverse+forward).

| Parameter | Φ_g | m | Total on m |
|-----------------|----------|-------|--------------|
| $\alpha = 0.13$ | -1.4 | +0.1 | -0.04 |
| $\alpha = 0.20$ | +1.4 | +0.1 | +0.04 |
| $\beta = 0.138$ | +0.3 | -0.01 | +0.02 |
| $\beta = 0.175$ | -0.3 | +0.01 | -0.02 |
| $a : -10\%$ | -0.3 | +0.07 | +0.05 |
| $a : +10\%$ | +0.3 | -0.07 | -0.05 |

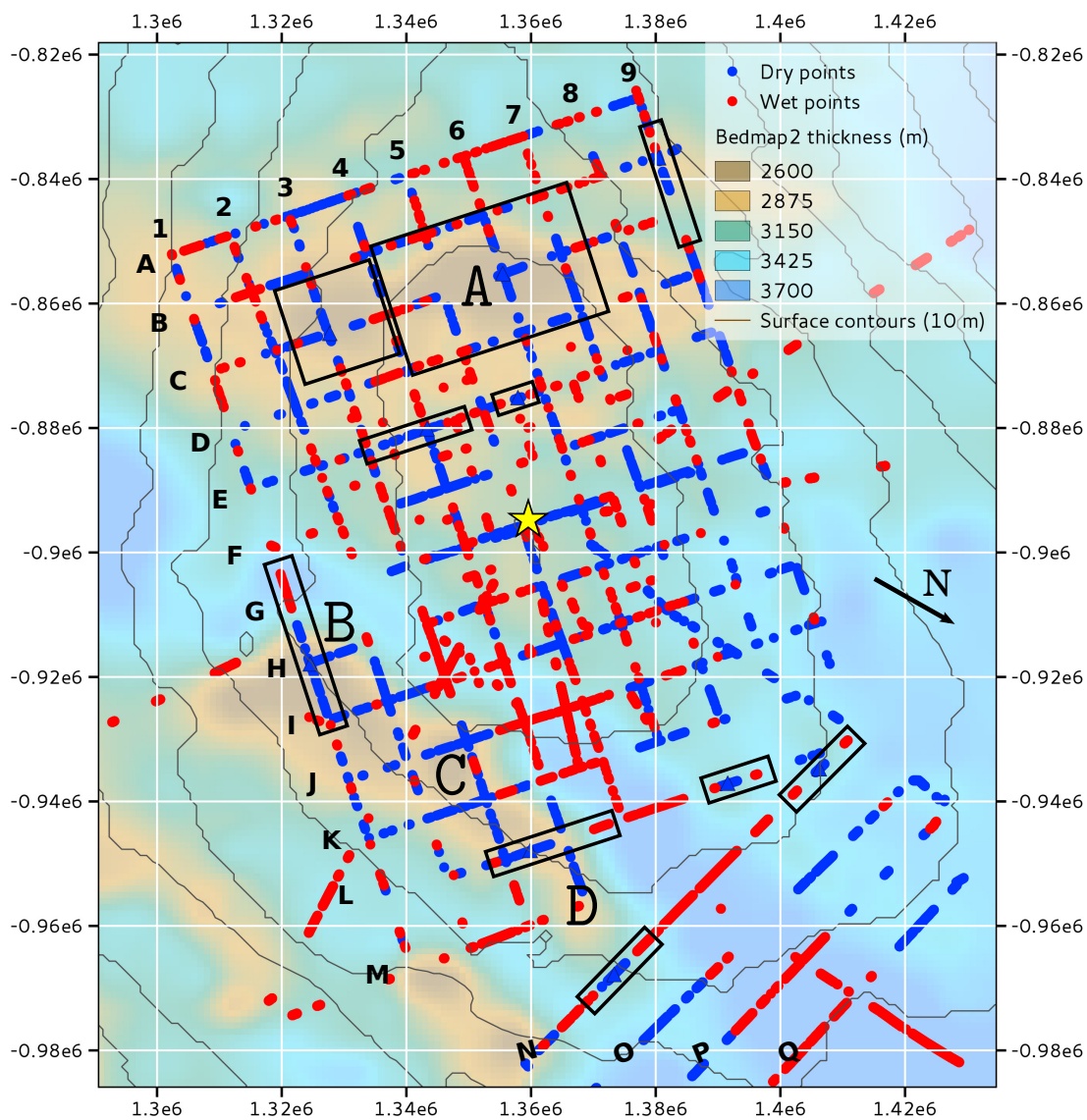


Figure 1. Wet and dry points (resp. blue and red), adapted from Zirizzotti et al. (2012). The yellow star shows the EPICA drill site, distant from the topographic dome by 1.4 km. Side numbers and letters are used to locate any intersection point on the radar grid. Large-size letters stand for the main sites of interest (candidates A, B, C and D). Projection: WGS84/Antarctic Polar Stereographic - EPSG:3031 (m). The north direction is bottom right.

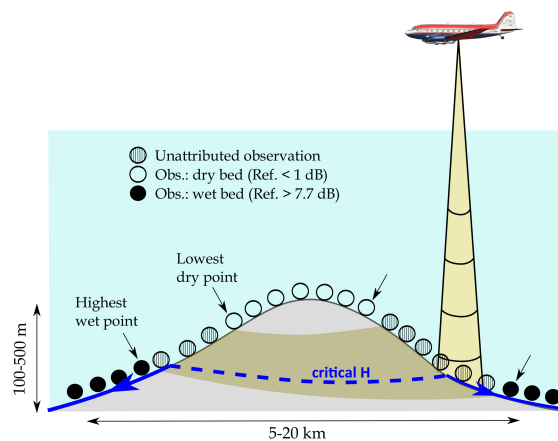


Figure 2. This figure illustrates how water and basal topography are linked in a region of flat surface for a uniform local GHF. The blue line shows the presence of water at the bed, and the direction of its flow. The brown area corresponds to a strip of unknown thermal conditions.

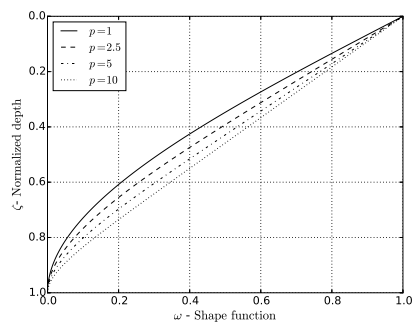


Figure 3. Shape function $\omega(\zeta)$ for several values of p (no basal melting).

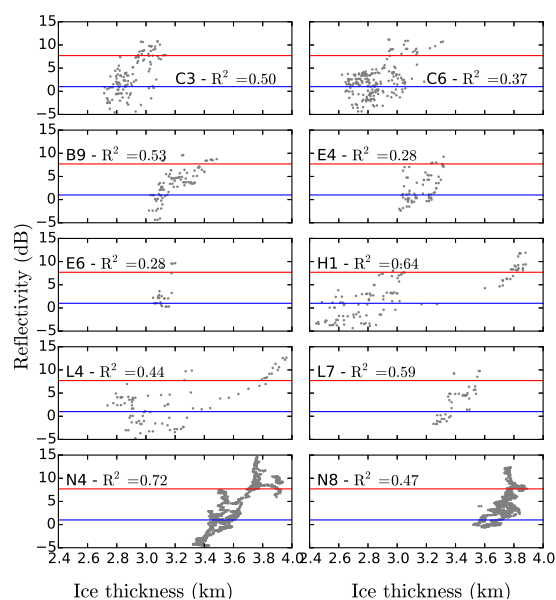


Figure 4. Basal reflectivity (dB) vs. ice thickness (km), on ten favourable spots. Red and blue lines correspond to the thresholds of wet and dry points.

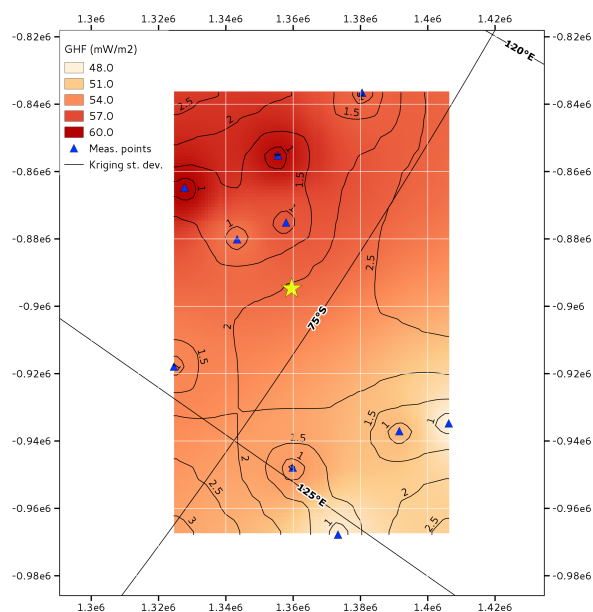


Figure 5. Geothermal heat flux, interpolated between the spots (blue triangles), and kriging standard deviation.

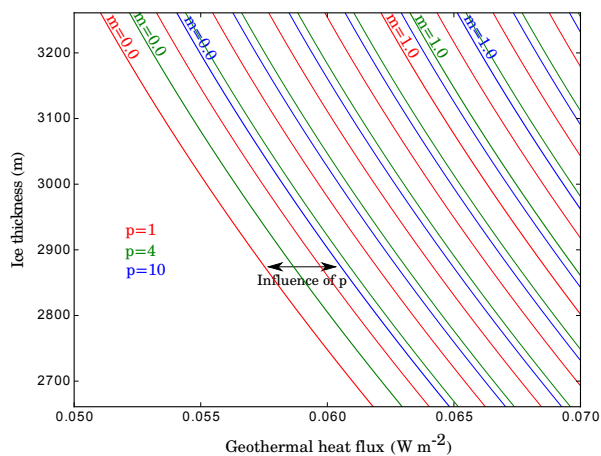


Figure 6. Basal melt rate in mm a^{-1} , depending on ice thickness, geothermal heat flux and p parameter.

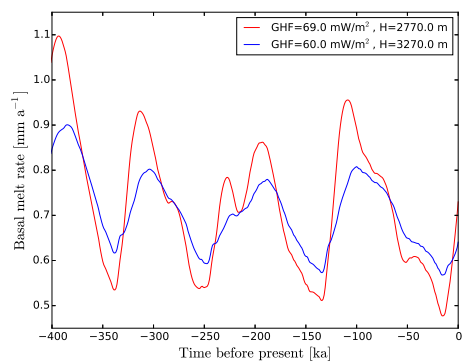


Figure 7. Evolution of the basal melt rate, depending on ice thickness and geothermal heat flux.

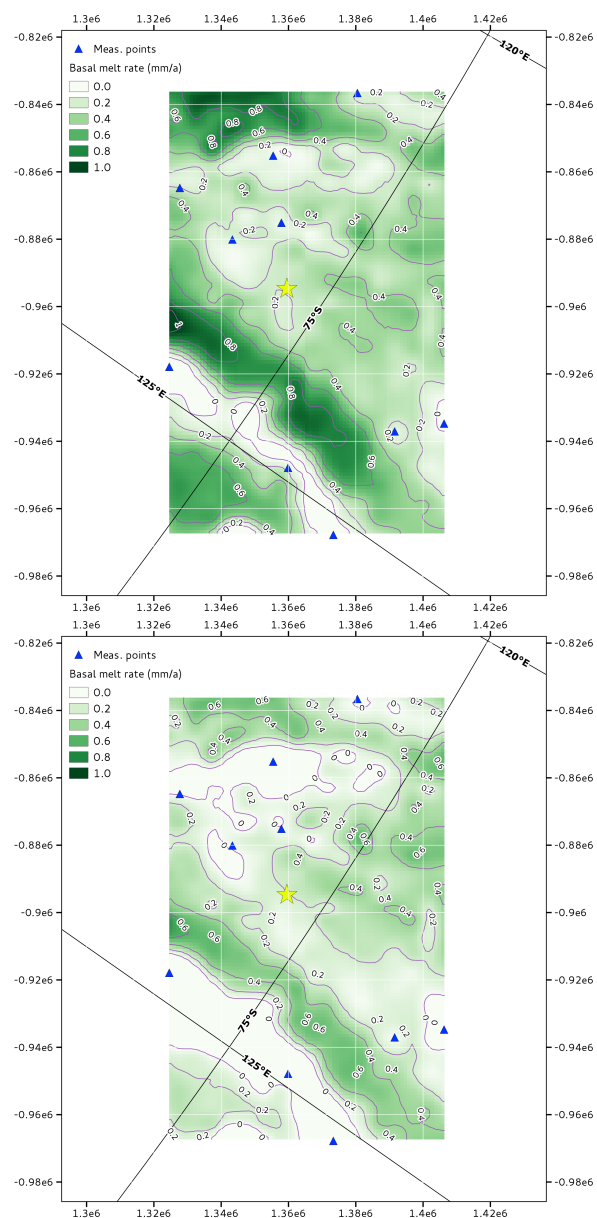


Figure 8. Top: basal melt rate in mm a^{-1} , inferred from the emulating polynomial function with $\hat{\Phi}_g + 2\sigma_\Phi$, and corresponding $p = 4.4$. Bottom: with $p' = p' - 2\sigma_p$ and corresponding GHF field. The ice thickness DEM is taken from the Bedmap 2 dataset (Fretwell and coauthors, 2013).

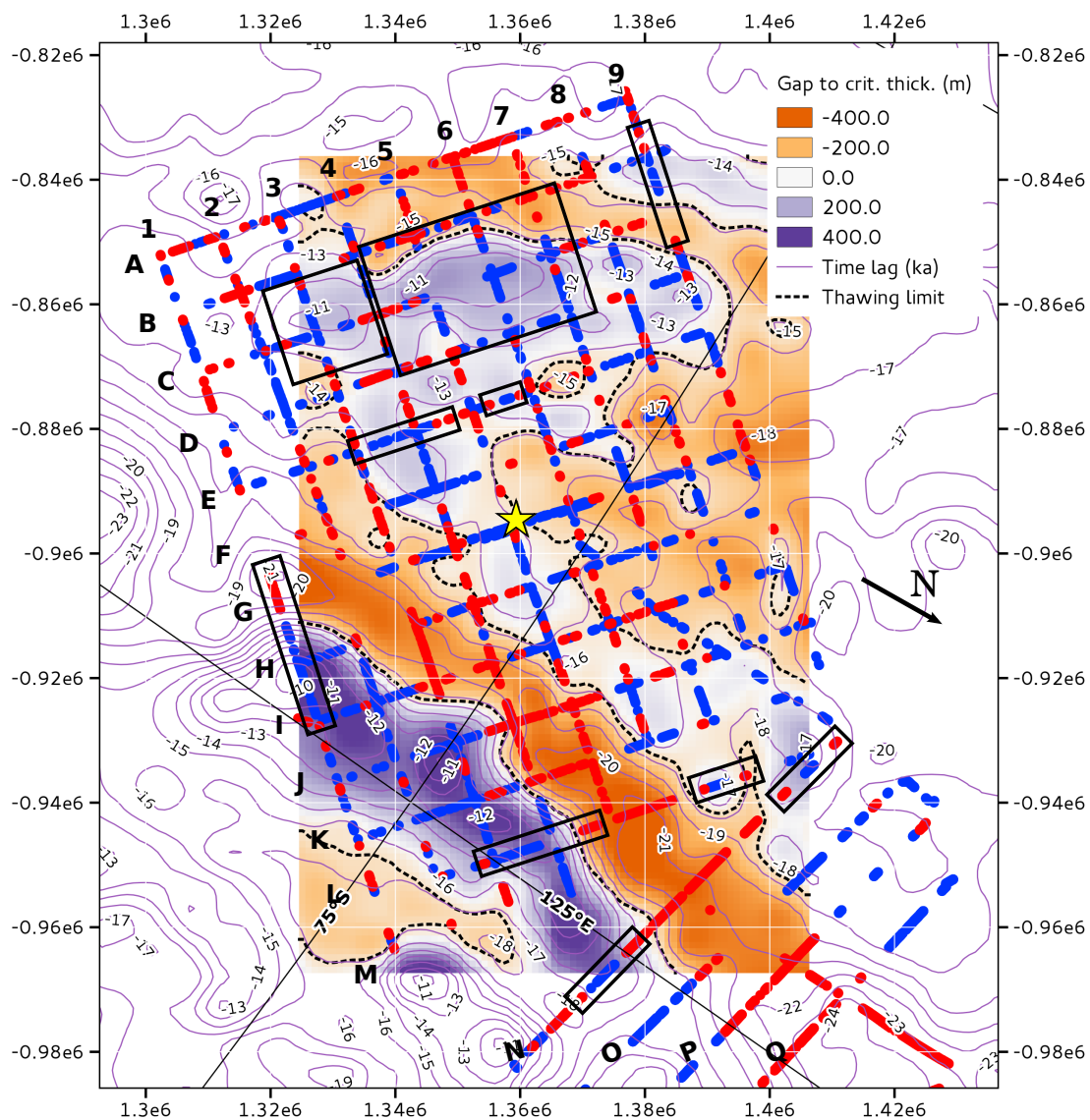


Figure 9. Difference between emulated critical ice thickness and observed ice thickness, done for $p = 2$ and $\Phi_g = \hat{\Phi}_g^m - 1 \text{ m W m}^{-2}$. The ice thickness DEM is taken from the Bedmap 2 dataset (Fretwell and coauthors, 2013). Isocontours show the time lag for the climatic signal to reach the bed.